JOURNAL OF MATERIALS SCIENCE 28 (1993) 3645–3652

Acoustic microscopy of ceramic-fibre composites

Part II Glass–ceramic-matrix composites

C. W. LAWRENCE, G. A. D. BRIGGS
Department of Materials, Oxford University, Parks Road, Oxford, OX1 3PH, UK
C. B. SCRUBY
AEA Industrial Technology, Harwell Laboratory, Oxon, OX11 0RA, UK

Two silicon-carbide-fibre composites, one with a magnesium-aluminosilicate matrix and the other with a calcium-aluminosilicate matrix, were studied using acoustic microscopy. Contrast was found between the fibres and the matrix, and there was, in addition, a distinctive contrast associated with the boundary between them. In some cases the contrast at the boundary was characteristic of a well-bonded interface, and in others it was characteristic of a crack; strong contrast was also found from cracks in both the matrix and the fibres. It was possible to obtain a good quantitative fit between observation and theoretical calculations of boundary contrast. Radial cracks and radial variations of the microstructure in the fibres were studied. From measurements of fringes in the areas of contrast and estimates of Poisson's ratio, values of the shear modulus and Young's modulus could be deduced; independent values from nano-indentation measurements were in good agreement. Some of the calcium-aluminosilicate composites were studied after straining below and beyond the elastic limit; and the appearance of cracks was related to a theoretical model, yielding a value for the interfacial strength within the range of reported values.

1. Introduction

The purpose of the work described here was to study composites of ceramic fibres in a glass–ceramic matrix by acoustic microscopy, in order to observe those properties of the composites relevant to their development and performance. These composites have both higher strength and higher toughness than the matrix material alone, offering materials with good performance up to 900 °C, and potentially up to 1100–1200 °C [1]. Glass–ceramics are polycrystalline solids produced by the controlled crystallization of glasses [2]; they have the advantage that at high temperatures before they are cerammed they have a low viscosity, so that good penetration and densification are possible in the fabrication of the composite [3, 4]. By adding appropriate nucleating agents and by controlled heat treatment of the glass, stronger crystalline phases can be produced. Over 90% of the parent phase can be crystallized in this way, and the higher temperature performance limit of the glass–ceramic, compared to the glass, comes from this polycrystalline nature. The composition of the parent glass can be chosen to give optimum compatibility with the fibres. In particular, the thermal expansion characteristics of the matrix can, in principle, be tailored to match those of the fibres, in order to prevent, or at least reduce, residual thermal stresses.

The two materials examined in this study were magnesium-aluminosilicate reinforced with silicon-carbide fibres, and calcium-aluminosilicate also reinforced with silicon fibres. The preparation for acoustic microscopy was identical to the description in part I; great care was again taken to ensure that the surface examined was representative of the specimens themselves, and not simply of the preparation technique. The acoustic microscope used for these studies was a Leica ELSAM, capable of operating up to 2 GHz, at which the resolution is 0.7 μm. In the materials studied here, a dominant role is played by Rayleigh waves excited in the surface of the specimen [5]. The contrast due to the Rayleigh waves varies with defocus (the distance by which the specimen is moved towards the lens relative to focus, denoted by $-z$), and it depends also on the Rayleigh velocity in the specimen (which in turn depends on the density and the elastic constants). Strong contrast is also to be expected when the Rayleigh waves are scattered by interfaces or cracks, and this is characterized by fringes spaced half a Rayleigh wavelength apart. These fringes are a familiar feature of the acoustic micrographs.

2. Magnesium–aluminosilicate/SiC (MAS/SiC)

Composites with a magnesium–aluminosilicate (MAS)

0022–2461

TABLE I Mechanical and thermal properties of SiC fibres and glass–ceramic-matrix materials

Property	Nicalon SiC fibres	Tyranno SiC fibres	Sigma SiC mono-filaments	MAS	CAS
Nominal composition (wt %)	Si 59 O 10 C 31	Si 47 Ti 2 O 18 C 33	Stoichiometric SiC on W core	SiO_2 51.3 Al_2O_3 34.9 MgO 13.8	SiO_2 42.8 Al_2O_3 36.2 CaO 20 As_2O_3 1
Density, ρ ($kg\,m^{-3}$)	2550	2300–2400	3040	2700	2860
Mean Diameter (μm)	16	8–10	100	–	–
Young's modulus, E (GPa)	196	206	420	110	106
Poisson's ratio, ν	–	–	0.2	0.25	0.26
Tensile strength (GPa)	2.75	2.74	3.60	0.15	–
Thermal expansion coefficient, α ($10^{-6}\,°C^{-1}$)	3.5 (20–300 °C)	3.1 (20–500 °C)	1.5	4.6 (20–1000 °C)	5.3 (20–1000 °C)
Maximum operating temperature (°C)	1000	1000	900	1200	> 1000

matrix were studied with two different kinds of fibre reinforcement. The first contained small Tyranno silicon-carbide fibres, denoted by a subscript t. The second had much larger sigma-silicon-carbide monofilaments, denoted by subscript m. The manufacture of the composites was proprietary, but from the published literature [6] it may be expected that the fabrication temperature was in the range 1200–1400 °C, with pressures of 7–14 MPa applied for up to 20 min. The matrix powder was magnesium-aluminosilicate glass with a small amount of glass ceramic added to initiate crystallization, together with ZrO_2 as a nucleating agent and Nb_2O_5 to give barrier protection to the SiC fibres. Mechanical and thermal properties of the two kinds of fibre are summarized in Table I, together with the corresponding properties of the glass–ceramic matrices. X-ray diffraction (XRD) indicated the matrix predominantly consisted of cordierite.

2.1. MAS/SiC_t

The microstructure of the matrix of the MAS/SiC_t composite can be seen in the acoustic micrograph in Fig. 1. There are two phases. The majority phase is darker than the minority phase at this Defocus, $z = -1$ μm (and also at focus); the minority phase occupies a volume fraction of about 15%. There is also a fine dispersion of porosity of diameter 1–2 μm, comprising approximately 2% of the volume fraction of the matrix. This volume fraction was confirmed by reflected-polarized-light microscopy, which also confirmed that the majority phase was crystalline and that the minority phase was glassy. The polarized-light microscopy was not able to elucidate further the nature of the fine dispersion of porosity. Both optical and acoustic microscopy of the composite indicated a fibre volume fraction of 0.4, with excellent distribution

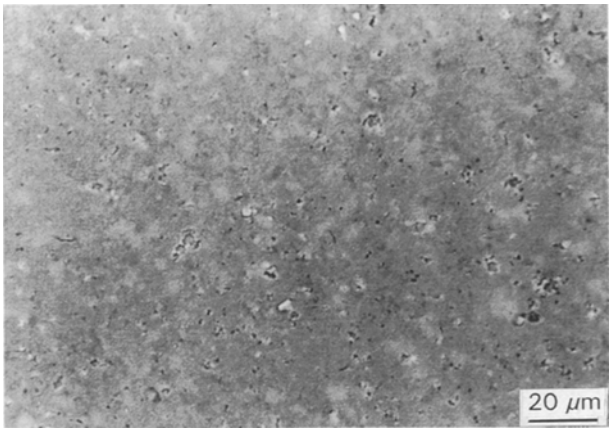

Figure 1 Acoustic micrograph of the matrix of MAS/SiC_t (Tyranno reinforcing fibres) for 1.9 GHz, and $z = -1.0$ μm.

and almost no fibre bunching at this low volume fraction.

The nature of the composite in cross-section is shown in Fig. 2, which is a series of images of the same area at increasing defocus. At focus in Fig. 2a, the fibres appear white; they have an average diameter of 9 μm, consistent with Table I. The matrix shows two phases, just as it did in the lower-magnification acoustic micrograph of Fig. 1. The minority phase is lighter than the rest of the matrix, with an average grain size of approximately 6 μm. Light fringes can be seen around the fibres. At a defocus of -1 μm, in Fig. 2b, the contrast is much more dramatic. First, it can be seen that even a change of 1 μm in the defocus has reversed the contrast of the fibres from light to dark. This is a manifestation of the well known $V(z)$ effect [7]; it is a caution against interpreting contrast in acoustic images naïvely. One cannot simply associate bright contrast with high density or high elastic stiffness, though both of these affect the contrast. Detailed

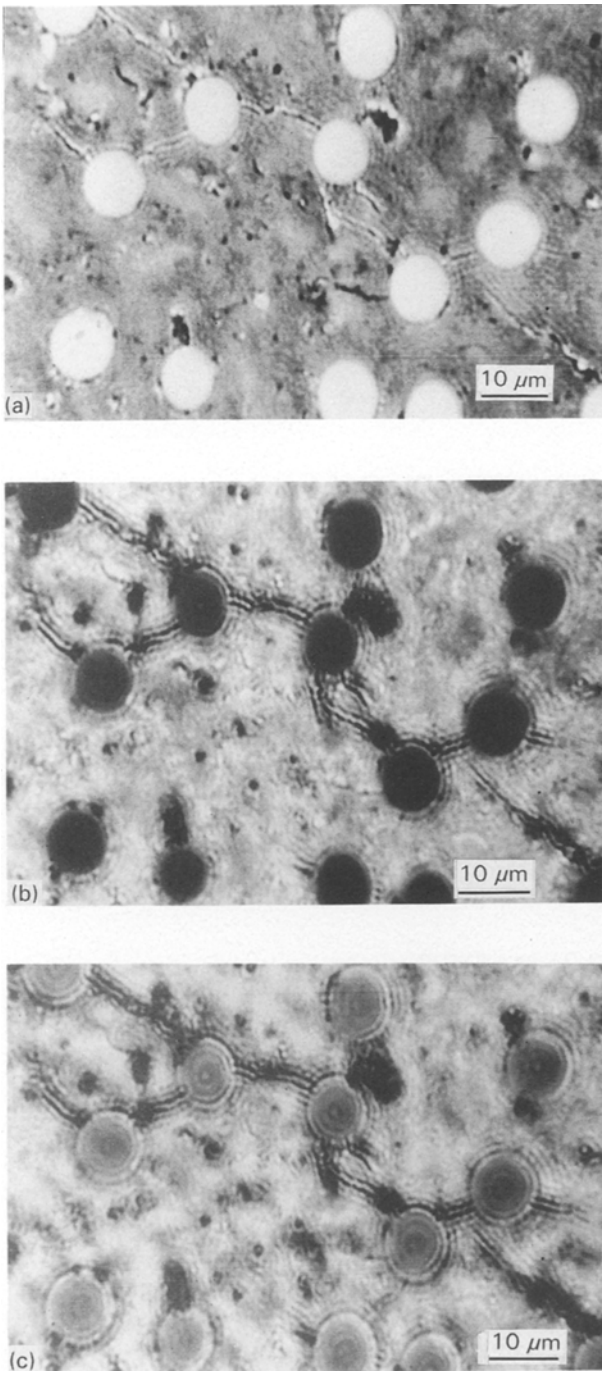

Figure 2 Acoustic micrograph of the MAS/SiC_t microstructure. Note in particular the extensive matrix microcracking between fibres for 1.9 GHz and: (a) $z = 0$, (b) $z = -1.0$ μm, and (c) $z = -2.0$ μm

interpretation must be performed in the light of the behaviour of the oscillations in $V(z)$ and their dependence on parameters that determine Rayleigh-wave propagation [8]. Secondly, the fringes around the fibres have become stronger with respect to the background matrix contrast. These fringes are a manifestation of the scattering of Rayleigh waves at the interface between two materials of different acoustic properties [9]. As the lens travels parallel to the surface in the course of its scan, the path length of Rayleigh waves that are reflected from the fibre–matrix interface changes, but the path of rays that are geometrically reflected from the surface remains constant. The interference of these two components at the transducer leads to the fringes that are seen here.

Finally, and perhaps most striking of all, there is remarkably strong contrast from cracks that run through the matrix between the fibres. These cracks can also be seen in Fig. 2a, but their contrast is greatly enhanced at the defocus of Fig. 2b. This sensitivity to cracks is because even when the width of the cracks is much less than the microscope's nominal spatial resolution Rayleigh waves propagating in the surface can, nevertheless, be strongly scattered. Two kinds of scattering, as perceived by the nature of the fringe contrast, can be seen in Fig. 2b. In the fringes along the cracks in the matrix the contrast extends from almost full black to full white, i.e. the through full range of the grey scale; whereas around most of the circumference of the fibres the contrast is somewhat more subdued. But around some parts of the fibre–matrix interface the contrast is more characteristic of a crack. This is noticeable, for example, around the top of the three most central fibres. Following the course of the various segments of crack suggests that these are places where a crack has been deflected by (or has nucleated at) a fibre, and that what is being seen are regions of the fibre–matrix interface where debonding has occurred, and where Rayleigh waves are being scattered just as they would be by a crack. This impression is confirmed by Fig. 2c, which is at twice the defocus of Fig. 2b. Here the cracks in the matrix are characterized by bright contrast at the crack itself, with at least one dark fringe either side. It would therefore be expected that a fibre–matrix debond would be characterized by a bright fringe with a dark fringe on the matrix side (the fibre side of the debond might be quite different, because it is a different material, but there are no cracks inside the fibres here to compare with), this is exactly what is seen, with very pleasing correspondence between where the cracks appear to go around the fibres in Fig. 2b and Fig. 2c.

The fringes in the matrix and in the fibre in Fig. 2c can be measured to deduce the Rayleigh velocity. The spacing of the fringes is $\Delta x = \lambda_R/2$, where λ_R is the Rayleigh wavelength. Therefore if the acoustic frequency is f then the Rayleigh velocity is

$$v_r = 2f\Delta x \quad (1)$$

Measurement of the fringes in Fig. 2 gives Rayleigh velocities of 3520 $m\,s^{-1}$ for the MAS, and 5150 $m\,s^{-1}$ for the Tyranno SiC. It is possible to make independent measurements of the Rayleigh velocity by analysing the oscillations in $V(z)$ in a line-focus-beam microscope [10]; measurements in this way yielded a Rayleigh velocity of 3550 $m\,s^{-1}$ for MAS. The Rayleigh velocity is related to the density and the elastic constants by a sextic equation involving both the longitudinal and the shear bulk velocities [5]. It is therefore not possible to deduce the elastic constants, even when the specimen is isotropic and the density is known, from the Rayleigh velocity alone. However, it is possible to write the Rayleigh velocity in terms of the density, ρ the shear modulus, G, and an approximate polynomial expansion in Poissons ratio, ν,

(Scruby *et al.* [11]),

$$v_r \approx \frac{1}{R_\nu}\left(\frac{G}{\rho}\right)^{1/2} \quad (2)$$

where $R_\nu \equiv 1.14418 - 0.25771\nu + 0.126617\nu^2$.

R_ν varies only slowly with ν, for example when $\nu = 0.15$, $\partial R_\nu/\partial_\nu = -0.207$. Thus if Poisson's ratio is known to be, say, 0.15 ± 0.01 (an uncertainty of 5%), the shear modulus can be deduced from the Rayleigh velocity to an accuracy of 0.4% (plus any error in the measurement and in the value of the density). The Poisson's ratio of Tyranno silicon-carbide fibres has not been measured, though a value of 0.15 has been quoted for the similar Nicalon fibre (see Part I [12]). For $\nu = 0.15$, $R_\nu = 1.108$. For the Tyranno fibre, $\rho = 2350\ \mathrm{kg\,m^{-3}}$ (Table I), and so from the measured Rayleigh velocity of $5150\ \mathrm{m\,s^{-1}}$, a shear modulus $G = 77$ GPa can be deduced. Similarly for the MAS, with $\rho = 2500\ \mathrm{kg\,m^{-3}}$ and $\nu = 0.25$, a mean Rayleigh velocity of $3535\ \mathrm{m\,s^{-1}}$ yields a shear modulus of 37 GPa.

The Young's modulus, E, of an isotropic material is related to the shear modulus and Poisson's ratio by

$$E = 2G(1 + \nu) \quad (3)$$

Hence a determination of E can be more sensitive to an error in ν, and an estimate of $\nu = 0.2 \pm 0.01$ would give an uncertainty of 0.46% in E (including the uncertainty in G, which is of opposite sign). The Young's modulus deduced for the Tyranno fibres in this way is $E = 177$ GPa, and $E = 93$ GPa for the MAS. For comparison, the *in-situ* Young's elastic modulus of the Tyranno fibres was measured using a nano-indenter. Using the simple analysis of Doerner and Nix [13] the elastic modulus of the fibres were determined to be 166 GPa with a standard deviation of 13 GPa (from 25 measurements), in satisfactory agreement with the acoustically derived value. Whilst more precise analyses have recently become available [14, 15] for load–displacement data from nano-indentation machines, the measured value is consistent with values determined by Pysher *et al.* [16] and Fishbach *et al.* [17] from tensile testing: 150 GPa and 171 GPa, respectively. Note that, unlike the tensile testing measurements, both the nano-indenter and acoustic-microscope measurements are not gauge-length dependent. These figures are not intended to be definitive, but they do illustrate the kind of measurement that can be made using an acoustic microscope.

The mean linear thermal-expansion coefficient of magnesium-aluminosilicate is $4.6 \times 10^{-6}\ ^\circ\mathrm{C}^{-1}$ (20–1000 °C), compared with $3.1 \times 10^{-6}\ ^\circ\mathrm{C}^{-1}$ for the Tyranno-SiC fibres (Table I). Hence the fibre–matrix interface will be in radial compression, while the matrix will be in longitudinal and circumferential tension. Putting these values into Equations 3–6 of Part I [12] (which explicitly include the radial decay of the thermal stress generated in the matrix) and assuming a hot-pressing temperature of 1300 °C, the axial thermal stress is 111 MPa and the matrix thermal hoop stress is 158 MPa and the radial thermal stress is −69 MPa. The matrix monolithic tensile strength is 138 MPa [18], and if there are local variations of the stresses because the distribution of the fibres is not completely uniform, then it is quite plausible that the microcracking is a direct consequence of the failure to match the thermal parameters of the fibre and the matrix. The way that the cracks follow the interface between fibre and matrix suggests that the interface is weaker than either the matrix or the fibre, and so fails preferentially; this in turn suggests that the matrix is indeed essentially crystalline with a comparatively fine grain size.

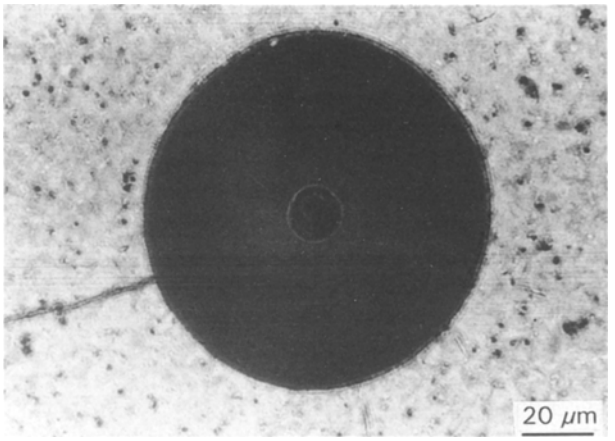

Figure 3 Acoustic micrograph of MAS/SiC_m (sigma-monofilament reinforcement) for 1.9 GHz, and $z = -4.6$ μm

2.2. MAS/SiC_m

An acoustic picture of a transverse section through a Textron monofilament in a MAS matrix is shown in Fig. 3. There is one long radial crack in the eight o'clock position, which was also seen without difficulty in a light microscope. There are two smaller radial cracks between four o'clock and six o'clock, and there may even be another crack between three and four o'clock; these cracks were not detected in the light microscope. They are identified in the acoustic micrograph by their characteristic fringe patterns. The residual thermal hoop stress may again be calculated using Equation 5 from [12] and the data in Table I; these give a tensile hoop stress of 392 MPa, a radial thermal stress of −210 MPa and an axial thermal stress of 286 MPa. Both the axial and hoop thermal stresses are greater than the matrix strength and so would explain the formation of the observed radial cracks.

Not all ring patterns are due to Rayleigh-wave scattering and interference. Fig. 4 shows the microstructure of a sigma-monofilament, at a somewhat higher magnification than Fig. 3 (and at a different defocus). The central core is a 14 μm diameter tungsten fibre. Onto this core β-SiC is deposited to give radial columnar grains. The concentric rings in the fibre are not due to interference. A simple analysis of their spacing via Equation 1 would give a surface-wave velocity of $24\,000\ \mathrm{m\,s^{-1}}$, which is faster than any known elastic wave! Besides, the rings do not have the appearance of interference fringes. It therefore seems that the rings reveal regions of different microstructure due to fluctuating SiC-deposition rates during the

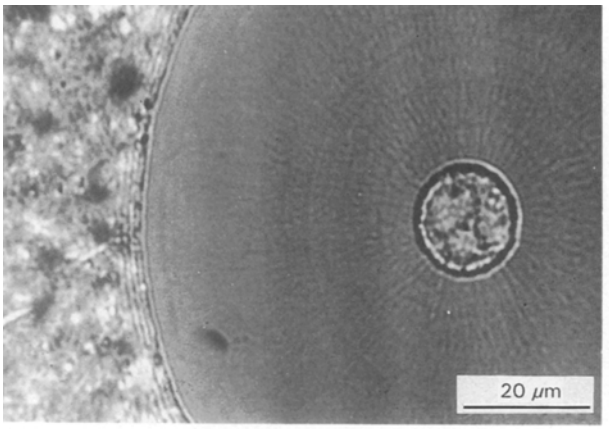

Figure 4 Acoustic micrograph of MAS/SiC_m for 1.9 GHz, and $z = -2.0$ μm. The vertical magnification is slightly greater than the horizontal magnification.

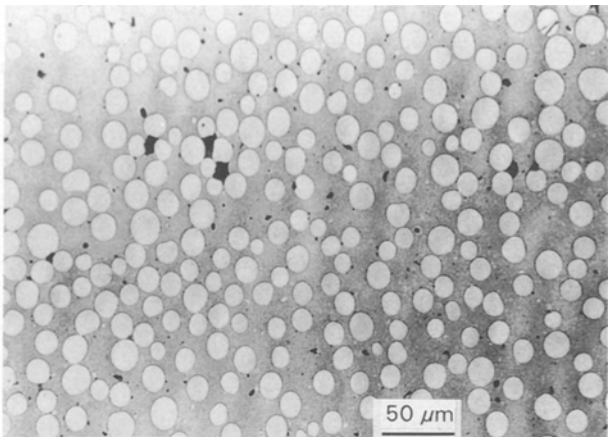

Figure 5 Acoustic micrograph of CAS/SiC (Nicalon reinforcing fibres) for 1.9 GHz, and $z = 0$.

fabrication of the monofilament. The fringes in the matrix next to the interface are Rayleigh-interference fringes, and they can be analysed in exactly the same way as they were in the MAS/SiC_t composite.

3. Calcium-aluminosilicate/SiC (CAS/SiC)

3.1 Fabricated specimens

Calcium-aluminosilicate is a relatively simple glass-ceramic, forming stoichiometric anorthite, $CaAl_2Si_2O_8$. The proprietary specimens were made by hot pressing at a temperature in the range 1300–1400 °C. 1 wt % As_2O_3 can be added as a fining agent to thicken the interfacial carbon layer and improve its mechanical properties; a good interface consists of a layer of graphitic carbon 100 nm thick [19]. For low-temperature applications the performance of a CAS/SiC composite is comparable with a glass-matrix composite such as 7740/SiC (see Part I [12]), but because the matrix is crystalline it can be used up to temperatures of 1000 °C or so, approaching the composite fabrication temperature and the usable temperature limit of the fibres. Nicalon silicon-carbide fibres were used as the reinforcing phase (see Table I for properties). The microstructure of a transverse section of a CAS/SiC composite (Fig. 5) shows the fibres and their distribution, a reasonably uniform matrix, and some porosity. The volume fraction of the fibres is not completely uniform; an average value is 0.4. The uniformity of the matrix, as characterized by density and elastic homogeneity, could not be determined so directly optically; but this is something that the acoustic microscope can reveal readily.

Fig. 6 shows an individual fibre in the composite at higher magnification, at focus and at a defocus $z = -3.2$ μm. At focus, Fig. 6a, the fibre and the matrix can be seen, with the interface between them quite well delineated. Two radial cracks are present (at four and one o'clock), and faint fringes can be seen inside and outside the interface; but the contrast is relatively flat. It is much more dramatic in the defocused image, Fig. 6b. There is more contrast from the microstructure of the matrix, and the contrast from

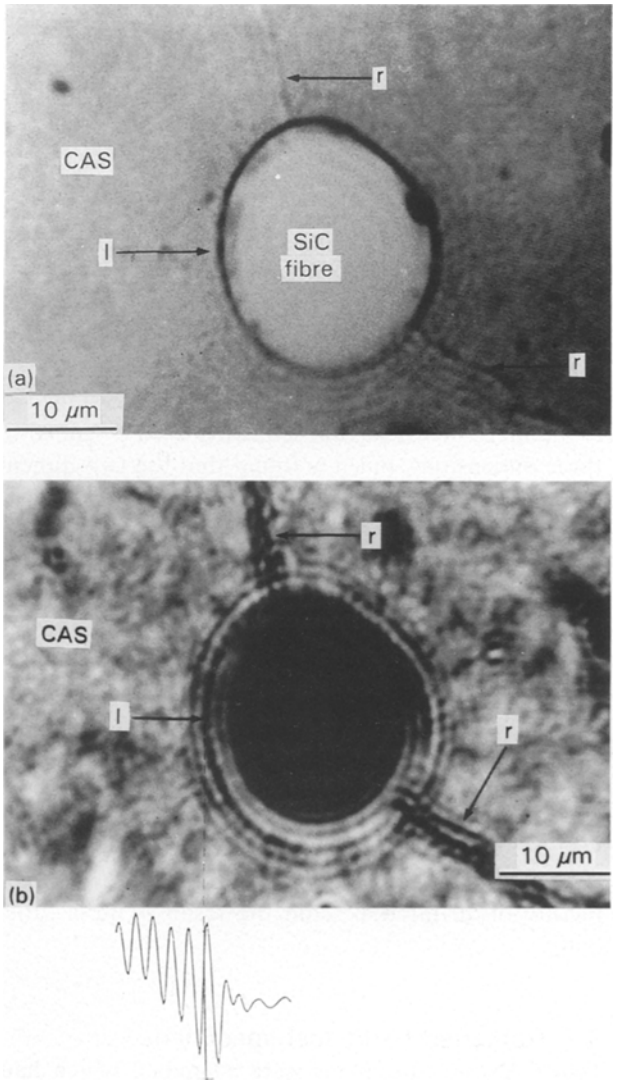

Figure 6 Acoustic micrographs of CAS/SiC for 1.9 GHz: (a) $z = 0$, and (b) $z = -3.2$ μm. The arrows labelled r indicate radial matrix microcracks, and the arrows labelled I indicate the fibre/matrix interface. The curve is a calculated linescan for the imaging conditions of (b), using the method in Chapter 12 of [10] and the material constants in Table 1.

the cracks is greatly enhanced, in the same kind of way that it was in Fig. 2. But there seems to be a problem: in the defocused image the fibre seems to have shrunk.

This is a perfectly genuine effect; there has been no change in the magnification. The dark region in the centre, especially towards the bottom of the picture, does not indicate the area of the fibre. The fibre actually extends two fringes further out, to the dark fringe indicated by I. A clue to this is given by the radial crack at five o'clock, which stops at the interface in Fig. 6a but stops short of the dark region in Fig. 6b (though the contrast at the end of the crack shows some further complications). Moreover the circular fringes associated with the interface show curious effects: they have one spacing and contrast outside the dark region, and then different contrast and spacing in the centre of the fibre; certainly not an abrupt change at the interface itself. If all this could be accounted for by a quantitative model, then that would add confidence to the interpretation that can be made of such micrographs, and also to the kind of distinction that was made in the discussion of Fig. 2 between the contrast from a crack and the contrast from an interface.

The contrast from the interface between two media has been analysed using a combination of ray theory and diffraction theory (Somekh et al. 1985 [20]). The materials on either side of the interface are characterized by their density and elastic properties, and the interface is characterized by transmission and reflection coefficients for Rayleigh waves; this has the great advantage that the results of calculations (often lengthy) from the literature for scattering of Rayleigh waves by different configurations can be immediately incorporated. The theory was originally developed in two dimensions; it has subsequently been extended to three dimensions, but it is found that the two-dimensional theory gives an adequate account of the behaviour of the contrast over a crack. A calculation has been performed, with no free parameters, for the situation in Fig. 6b, and the result is superimposed on the micrograph. The frequency and defocus used were the same as in Fig. 6b, and the materials parameters were taken from Table I. The calculated curve follows the changes reasonably well, not only in the level of the contrast, but also in the period of the oscillations. In particular, it exhibits an apparent sideways displacement of the interface in the same kind of way that the experimental image does. This is the first time that the theory had been so directly tested on a picture of an interface, and the result is quite satisfying.

3.2 Damaged bend-test specimens

Two CAS/SiC specimens were examined which had been deformed in a flexural test. In each case the specimen was held at a known strain; then a quick-setting resin was poured into a mould that was placed around it, with the aim of preventing the closure of any matrix microcracks generated during the deformation. The strain was parallel to the fibre direction. The first specimen was strained close to the elastic limit of the matrix, $\varepsilon = 0.235\%$; the second was strained beyond it, $\varepsilon = 1.25\%$. Longitudinal sections were then prepared for microscopy.

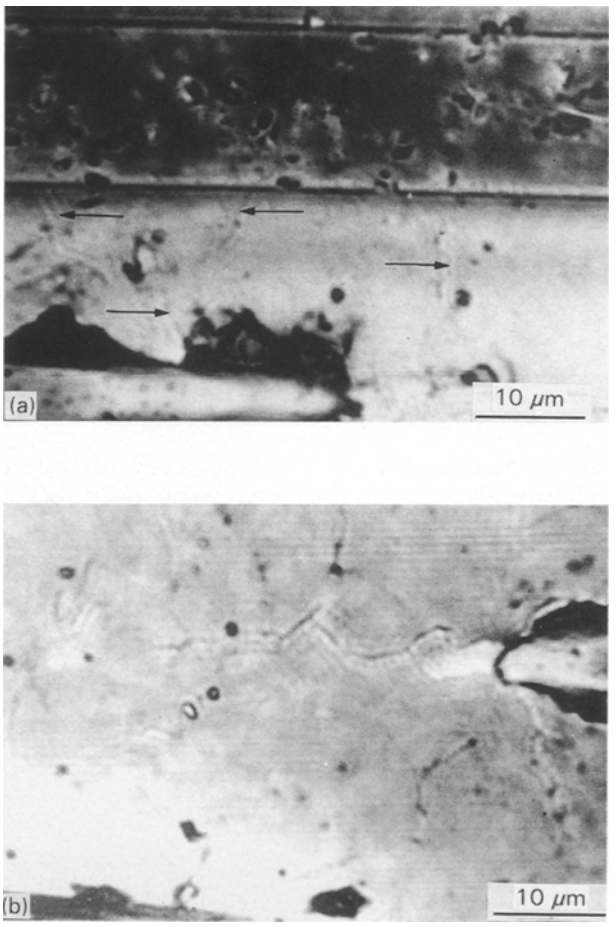

Figure 7 Acoustic micrographs of CAS/SiC bend specimen strained close to the elastic limit; $\varepsilon = 0.235\%$, 1.9 GHz: (a) $z = -1.0$ μm, the arrows indicate cracking between the fibres; and (b) $z = -0.8$ μm.

Acoustic micrographs of two areas of a section through the first specimen are shown in Fig. 7. In Fig. 7a there are a number of microcracks, indicated with arrows, that were not detected when this section was examined by an optical microscope. As usual, these cracks are characterized by Rayleigh fringes running alongside them. In many ways these cracks look similar to the cracks seen in the as-fabricated specimens in Fig. 5, although of course this is a different section, and the relative abundance is similar. But the cracks in the strained specimen tend to be longer, and in many cases they bridge closely spaced fibres. The strain may have caused inherent microcracks to propagate through the matrix until they were deflected by the fibres along the fibre–matrix interface. Cracks were also found parallel to the fibre axis throughout the specimen; an example is given in Fig. 7b. These cracks have the same orientation as the cracks seen in a transverse section, but since they invariably start where a fibre emerges from the section, it is feared that they are probably an artefact of section preparation. The difficulty of preparing these sections should not be underestimated, and it is remarkable that the other specimens are relatively free from such artefacts.

The specimen that had been strained beyond the elastic limit was much more interesting. Two acoustic micrographs of different areas at different magnifications are shown in Fig. 8. The fuzzy variations of

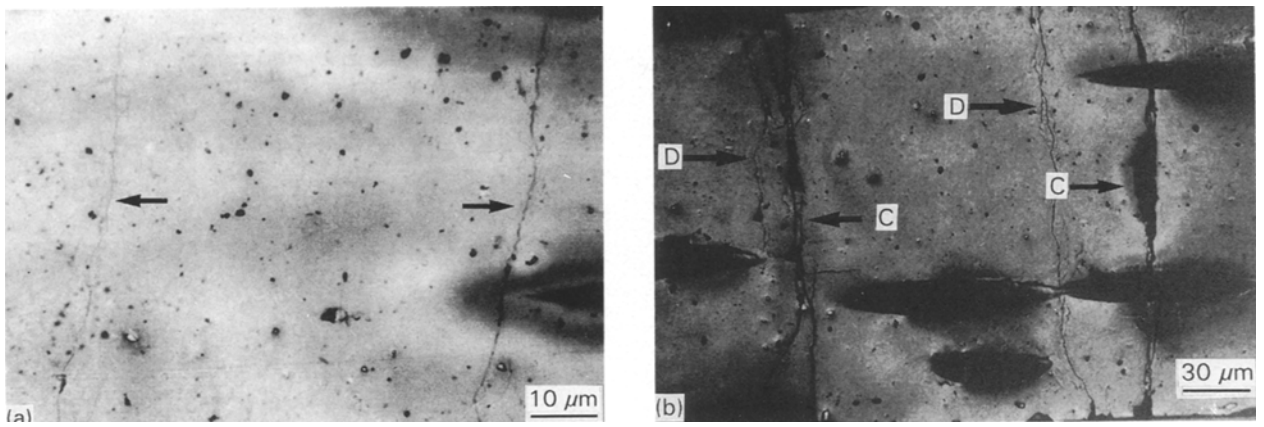

Figure 8 Acoustic micrographs of CAS/SiC bend specimen strained beyond the elastic limit; $\varepsilon = 1.25\%$, 1.9 GHz, $z = 0$. (a) The arrows indicate minor (closed) microcracks; and (b) the arrows labelled C indicate open cracks described by the Aveston, Cooper and Kelly theory [21], and the arrows labelled D indicate closed cracks.

contrast are due to the $V(z)$ effect where the surface is not quite flat. Fig. 8a is part of the beam that was in compression. The cracks are again similar to what was seen in the as-fabricated material, though the orientation is different. Rayleigh fringes were seldom seen beside these cracks, suggesting that they may be subject to closure stresses. In a tensile region in Fig. 8b, the appearance is quite different. Once again there are fine cracks perpendicular to the fibres (labelled D), which again may have been there before the deformation. There are also cracks (labelled C), that were sufficiently wide to show that the fracture surfaces had separated. Like the other cracks, these were probably intergranular; but they often bifurcated with the subsidiary cracks propagating parallel to the main crack, and occasionally rejoining it.

The limiting crack spacing, which varies from X to $2X$, can be related to the composite stress σ_{mc} at which cracking first occurs by the Aveston, Cooper and Kelly model [21]. If R is the fibre radius, τ_f the interfacial frictional shear strength (IFSS), E and V are the Young's modulus and volume fraction, where the subscripts f and m denote fibre and matrix, then the crack spacing X is given by

$$X = \left(\frac{\sigma_{mc} R}{2\tau_f V_f}\right)\left(\frac{E_m V_m}{E_m V_m + E_f V_f}\right) \quad (4)$$

where X is equal to 1.364 times the measured mean crack spacing (125 μm with a standard deviation of 51 μm). Putting the appropriate fibre and matrix properties into Equation 4 yields a value for the IFSS of $\tau_f = 6.3$ MPa. If the *in-situ* measurements of the elastic properties of the fibre and matrix ($E_m = 76$ GPa and $E_f = 184$ GPa measured using a nano-indenter) are used, the deduced IFSS rises slightly to 8.6 MPa. Both values lie within the range of reported values [22].

4. Conclusion

There have been many uses of acoustic microscopy at lower frequencies for detecting cracks inside composites [23]; for crack detection it can for some purposes be regarded as a high resolution non-destructive testing (NDT) technique. But in the studies presented here acoustic microscopy is playing a quite different kind of role. It is being used to characterize the materials in a way that would be relevant for understanding their properties, and perhaps improving them. The acoustic waves that are important here are not bulk waves that propagate down into the interior, but rather Rayleigh waves that propagate along the surface. The properties of the CAS/SiC and MAS/SiC composites to which the acoustic microscope has shown special sensitivity include the microstructure of both matrix materials, the microstructure of the sigma-monofilament, and cracking in the matrix and between the fibre and the matrix. Perhaps most important of all, it has been possible to make an accurate calculation of the contrast to be expected from interfaces that are bonded (and those that are debonded, corresponding to a crack between them), and to use this to interpret the contrast from a fibre–matrix interface or debond quantitatively. It is hoped that these studies will contribute to the use of acoustic microscopy for the study and development of advanced composite materials.

Acknowledgements

This work was undertaken while CWL was supported by SERC research studentship. CBS is an Industrial Fellow of Wolfson College. The ELSAM at Oxford is used in collaboration with Leica, Wetzlar; and we particularly wish to thank Mr K. Krämer. Material was kindly provided by Mr J. R. R. Davies of AEA Industrial Technology and Dr D. Dawson of Rolls–Royce plc.

References

1. R. W. DAVIDGE and J. J. R. DAVIES, *Int. J. High. Tech. Ceram.* **4** (1988) 341–58.
2. P. W. McMILLAN, in "Glass–ceramics" (Academic Press, London, 1964).
3. Y. IMANAKA, K. YAMAZAKI, S. AOKI, N. KAMEHARA and K. NIWA, *J. Ceram. Soc. Jpn.* **97** (1989) 309–13.
4. L. M. SHEPPARD, *Amer. Ceram. Soc. Bull.* **67** (1988) 1779–82.

5. G. A. D. BRIGGS, in "Acoustic microscopy" (Oxford University Press, Oxford, 1992).
6. B. L. METCALFE, I. W. DONALD and D. J. BRADLEY, *J. Mater. Sci.* **27** (1992) 3075–81
7. A. ATALAR, C. F. QUATE and H. K. WICKRAMASINGHE, *Appl. Phys. Lett.* **31** (1977) 791–3.
8. G. S. KINO, in "Acoustic waves–devices, imaging and analogue signal processing" (Prentice Hall, Englewood Cliffs, New Jersey, 1987).
9. K. YAMANAKA and Y. ENOMOTO, *J. Appl. Phys.* **53** (1982) 846–50.
10. J. KUSHIBIKI and N. CHUBACHI, *IEEE Trans. Sonics Ultrasonics.* **27** (1985) 189–212.
11. C. B. SCRUBY, K. R. JONES and L. ANTONIAZZI, *J. NDE* **5** (1986) 145–56.
12. C. W. LAWRENCE, C. B. SCRUBY, G. A. D. BRIGGS and J. R. R. DAVIES, *J. Mater. Sci.* **28** (1993) 3635.
13. M. F. DOERNER and W. D. NIX, *J. Mater. Res.* **1** (1986) 601–9.
14. W. C. OLIVER and G. M. PHARR, submitted to *J. Mater. Res.*
15. T. P. WEIHS, C. W. LAWRENCE and J. B. PETHICA, *J. Mater. Res.* **7** (1992) 1564–83.
16. D. J. PYSHER, K. G. GORETTA, R. S. HODDER and R. E. TRESSLER, *J. Amer. Ceram. Soc.* **72** (1989) 284–8.
17. D. B. FISCHBACH, P. M. LEMOINE, G. V. YEN, *J. Mater. Sci.* **23** (1988) 987–93.
18. Ceramic Source, Vol. 5, (The American Ceramic Society, OH, 1989).
19. R. F. COOPER and K. CHYUNG, *J. Mater. Sci.* **22** (1987) 3148–60.
20. M. G. SOMEKH, H. L. BERTONI, G. A. D. BRIGGS and N. J. BURTON, *Proc. Roy. Soc. Lond. A* **401** (1985) 29–51.
21. J. AVESTON, G. A. COOPER and A. KELLY, in: Proceedings of the National Physical Laboratory Conference on The Properties of Fibre Composites, Leuven, Belgium, 1971 pp. 15–26.
22. C. W. LAWRENCE, S. KOONER, T. P. WEIHS and B. DERBY, in "Interfacial phenomena in composite materials '91", edited by I. VERPOEST and F. JONES, (Butterworth–Heinemann, Oxford, 1991) p 208–11.
23. B. T. KHURI-YAKUB, P. REINHOLDTSEN and C.-H. CHOU, *IEEE Trans. Sonics Ultrasonics.* **27** (1985) 746–9.

Received 9 November
and accepted 10 December 1992